Anomaly detection in distributed electrical measurements using F-tests on a distribution grid model

Christian Dausel Jensen
AAU
Department of Electronic Systems
Aalborg, Denmark
fd60pj@es.aau.dk

Jakob Gulddahl Rasmussen
AAU
Department of Mathematical Sciences
Aalborg, Denmark
jgr@math.aau.dk

Rasmus Løvenstein Olsen
AAU
Department of Electronic Systems
Aalborg, Denmark
rlo@es.aau.dk

Somesh Bhattacharya
GridData GmbH
Anger, Germany
somesh@griddata.eu

Hans-Peter Schwefel
GridData GmbH
Anger, Germany
AAU
Department of Electronic Systems
Aalborg, Denmark
hps@es.aau.dk

Abstract

Anomaly detection in measurements within electrical distribution grids is essential for maintaining accurate state estimation and ensuring efficient grid management. This paper presents a novel anomaly detection framework that extends a linear state estimation model with statistical F-tests to identify deviations in distributed voltage or current phasor measurements. Assuming knowledge of the grid topology and correct phasor measurements, but subject to zero-mean complex Gaussian noise with known standard deviations, the anomaly detection approach checks whether deviations in measured data exceed normal fluctuations. The proposed algorithm flags potentially anomalous phasor measurements when the corresponding p-value from an F-test falls below a predefined significance level. Extensive simulations on a medium-voltage grid demonstrate the framework's ability to detect subtle magnitude and angle anomalies across a wide range of operating scenarios, maintaining robust performance even under reduced measurement coverage. The approach is scalable, interpretable, and well-suited for deployment in resource-constrained monitoring and data quality assurance within electrical distribution grids. *Code available at* `https://github.com/DauselJensen/F-testcode`

Keywords

Electrical measurements, anomaly detection, electricity distribution grids, hypothesis testing, stochastic grid state estimation, statistical grounded test

ACM Reference Format:
Christian Dausel Jensen, Jakob Gulddahl Rasmussen, Rasmus Løvenstein Olsen, Somesh Bhattacharya, and Hans-Peter Schwefel. 2025. Anomaly detection in distributed electrical measurements using F-tests on a distribution grid model. In *The 16th ACM International Conference on Future and Sustainable Energy Systems (E-ENERGY '25), June 17–20, 2025, Rotterdam, Netherlands.* ACM, New York, NY, USA, 11 pages. https://doi.org/10.1145/3679240.3734655

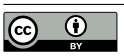

E-ENERGY '25, Rotterdam, Netherlands

ACM ISBN 979-8-4007-1125-1/25/06
https://doi.org/10.1145/3679240.3734655

1 Introduction

Modern power distribution grids are increasingly vulnerable to cyber threats. The integration of renewable and distributed energy resources, such as photovoltaic systems and wind turbines, introduces substantial complexity into the operation and planning of distribution grids. Accurate and timely state estimation, based on real-time phasor measurements, is needed for ensuring reliability, grid security, and operational awareness [2].

The cyber-physical structure of smart grids is subject to vulnerabilities. Measurement errors can arise not only from sensor failures and communication faults, but also from cyberattacks such as False Data Injection (FDI) or data manipulation from an attacker[1, 11, 14, 16], or mistakes such as wrong manual input [11], mechanical faults (e.g. sensor malfunction) [14], environmental interference [3, 16-20] or system errors due to power quality issues or unexpected loads [11]. As a consequence, particularly in distribution grids, where smart meters and μPMUs are deployed at scale with limited protection, these threats may compromise system observability, and lead to uninformed operational decisions [7].

Cyber attacks are a major threat for smart grids and may cause blackouts, service disruptions, or loss of trust, which can lead to large-scale economic damage. Examples are: STUXNET; one of the first documented cyber attacks reflecting physical damage, it delayed the Iranian nuclear programme by 5 years [1], "The Sandworm gang", Russian hackers created a power outage affected over 600,000 homes in Ukraine, WannaCry Ransomware; cost over £92 million in damages, repairs and upgrades in UK [5], and generally Non-Technical Losses in smart grids — which include cyber attacks — cause 96$ billion in revenue loss globally every year [7]

Existing anomaly detection methods leveraging deep learning models (e.g. convolutional autoencoders and LSTMs) effectively capturing complex patterns but typically demand extensive training data, have scalability limitations, and often operate as "black boxes," lacking interpretability [8, 14, 17]. These limitations make

them difficult to deploy regarding low-resource devices or sparsely monitored grids. Consequently, there is a clear research gap in anomaly detection surveys such as [14], [1], where they lack an interpretable, efficient anomaly detection framework that leverages physical grid constraints without extensive data requirements.

To address these challenges, building on the stochastic grid model introduced in [10], we propose a new anomaly detection framework that identifies individual phasor measurements whose deviations cannot be explained by normal measurement noise. Unlike the previous framework [10], which focuses on state estimation under Gaussian uncertainty, we extend the measurement model to perform statistically grounded detection of anomalous measurements using F-tests. This allows us to distinguish between ordinary noise and genuine anomalies. Furthermore, we leverage the projection structure introduced in [12], but go beyond it by proving that the relevant projection matrix is orthogonal, which is an essential condition for the validity of our statistical test. In this sense, the test provides a data-driven; nonetheless, physically grounded tool for detecting cyber-physical attacks without requiring attack-specific signatures or training data. The new framework offers an interpretable, efficient, and rigorous method for detection applicable to both fully and partially observed grids.

The remainder of this paper is structured as follows. Section 2 defines the system model and key assumptions. Section 3 introduces the anomaly detection framework, detailing the theoretical formulation of the F-test and its implementation. Section 4 describes the experimental setup, including the test grid, anomaly types, and evaluation metrics. Section 5 presents the results of the method under various anomaly magnitudes, measurement scenarios, and significance levels. Finally, Section 6 summarises the main findings, discusses limitations, and outlines directions for future work.

2 System model

The goal of this section is to define measurements, anomalies and general assumptions for the system model. This information will be a necessary prerequisite for understanding the anomaly detection framework in the next section.

We assume a synchronised set of phasor measurements taken at a single time instance for a medium-voltage (MV) distribution grid. The grid contains M nodes, each assigned a voltage phasor, and M lines, each assigned a current phasor, which collectively form the unknown true grid state vector $\mathbf{x} \in \mathbb{C}^N$, where $N = 2M$ is the total number of voltage and current phasors.

We assume that loads or generators are only connected to the leaf nodes of the tree. All topology assumptions are based on the industry, which shows most European DSOs now have GIS (Geographic Information systems) or NIS (Network Information Systems), in which at least the Medium-Voltage grids are represented with some good accuracy. Hence, it is assumed that the grid topology and line parameters are known. Given the grid assumptions, the state $\mathbf{x}$ must satisfy a set of physical constraints derived from Kirchhoff's current law (KCL) and Ohm's law:

$$Cx = 0, \tag{1}$$

where $C \in \mathbb{C}^{Q \times N}$ encodes the grid topology and line parameters. Here, Q is the number of linear equations, which are dependent on the number of grid lines and on the number of interior nodes in the graph for which Kirchhoff equations are formed.

At a given time instance, a subset of the state is observed through synchronised phasor measurements, forming the measurement vector $\mathbf{z} \in \mathbb{C}^K$, where $K \leq N$ is the number of observed phasors, referred to as measurements. The measurement model is

$$\mathbf{z} = D\mathbf{x} + \boldsymbol{\epsilon}, \qquad \boldsymbol{\epsilon} \sim CN(0, \Sigma_1, \Sigma_2), \tag{2}$$

where $D \in \{0,1\}^{K \times N}$ is a selection matrix indicating which true grid states are mapped to measurements, and the noise $\boldsymbol{\epsilon} \in \mathbb{C}^K$ is drawn from a complex normal distribution with zero mean, covariance matrix Σ_1, and pseudo-covariance matrix Σ_2 [10].

The measurement anomalies in this work are point anomalies, defined as an individual measurement that significantly deviate from expected values under normal grid operating conditions. Normal operations infer that the highest natural deviation a measurement can have, stems from the measurement noise model (Σ_1, Σ_2) and is assumed to be known or estimated based on [10]. Anomalies can arise from cybersecurity threats, with false data injection (FDI) attacks frequently highlighted as a critical threat category in smart grid cyber security literature [1][18]. However, the scope of this paper is not the detection of cyber threats, but rather the identification and analysis of their outcomes, specifically, the anomalies induced in the measurement data. Accordingly, the anomalies introduced into our dataset, detailed explicitly in Section 4, are inspired particularly by the anomaly types referred to as A4 and A5 in [18].

3 Anomaly Detection Framework

This section presents our anomaly detection framework for identifying individual measurements that deviate from the expected physical behaviour of the grid. The detection is performed using the linear measurement model and its associated constraints introduced in Section 2, where the true state $\mathbf{x}$ must satisfy the grid constraints $C\mathbf{x} = 0$, and the observed measurements $\mathbf{z}$ are subject to stochastic noise.

The core idea is to assess whether each measurement in $\mathbf{z}$ is statistically consistent with the physical model. To this end, we formulate a statistical F-test based on projections onto constraint-consistent subspaces. By comparing the system's behaviour under the full set of physical constraints to a reduced version where constraints involving $\mathbf{z}_k$ for $k = 1, \ldots, N$ are omitted, we test whether the observed deviation is likely due to random Gaussian measurement noise or indicates a genuine anomaly. This approach allows measurement-based hypothesis testing without relying on historical data, training labels, or complex black-box models. Furthermore, this detection method is focused on a single phase system for simplicity; nonetheless, the method allows for a 3-phase system using an extended version of the same approach.

We create an F-test for testing whether one or more chosen rows of C reasonably are fulfilled by the true state given the observed data. Denote by C_0 the matrix consisting of a chosen subset of the rows in C, and similarly let C_1 denote the matrix consisting of the rest of the rows. Furthermore, let Q_0 and Q_1 be the number of rows in C_0 and C_1, respectively. The selection of rows for C_0 is based on which constraints are *active* for a given measurement, i.e., the

nonzero rows of C. Formally, the set of active rows is defined as

$$\text{ActiveRows}(C) = \{i \in \{1, \dots, Q\} \mid \|C_i\| \neq 0\}, \tag{3}$$

where $C_i \in \mathbb{C}^{1\times N}$ denotes the ith row of C.

The hypothesis can therefore be formulated as

$$\mathcal{H}_0 : \text{The true state obeys the constraints } C_0\mathbf{x} = 0.$$

To perform this test, we define a projection matrix $\bar{H}$ based on the augmented system model in [12]. The formula for $\bar{H}$ and all the necessary matrix components in its formula, and complex-augmented notation/bar notation and derivations can be found in subsection A.4. Now, the distribution of the F-statistic is derived in the following proposition:

Proposition 3.1. *Assume that* (1) *and* (2) *holds. If T is the inverse of the principal square root of $\bar{\Sigma}$, $\bar{\mathbf{z}}_T = T\bar{\mathbf{z}}_T$, $\bar{H}_T = T\bar{H}T^{-1}$, and $\bar{H}_{1,T} = T\bar{H}_1T^{-1}$, then under $\mathcal{H}_0$*

$$F_T(\mathbf{z}) = \frac{\|\bar{H}_{1,T}\bar{\mathbf{z}}_T - \bar{H}_T\bar{\mathbf{z}}_T\|^2/\delta_1}{\|\bar{\mathbf{z}}_T - \bar{H}_{1,T}\bar{\mathbf{z}}_T\|^2/\delta_2}, \tag{4}$$

follows an F-distribution with degrees of freedom given by

$$\delta_1 = 2Q_0 \quad \textit{and} \quad \delta_2 = 2(K + Q_1 - N).$$

The proof can be found in Appendix A.8. This proof is built on Lemmas A.1 and A.2, which can be found in Appendix A.5 and A.6. Furthermore, details on the transformation T can be found in Appendix A.7. Finally, we have also derived a new and more efficient solution for $\bar{F}_{11}$, which is a key component within the maximum likelihood estimation framework for estimating the grid state in [12]. We can express it as a projection identity:

$$\bar{F}_{11} = (P_{\bar{C}}\bar{G}P_{\bar{C}})^{+},$$

where $P_{\bar{C}}$ is the orthogonal projection onto the nullspace of the constraint matrix $\bar{C}$, and $\bar{G}$ is the augmented measurement matrix. The proof can be found in Appendix A.10.

Having all necessary theoretical results, we can formulate the anomaly detection algorithm, see Algorithm Algorithm 1. For each measurement in $\mathbf{z}_k$, the corresponding state variable $\mathbf{x}_n$ is identified using the measurement matrix D. The algorithm then extracts all rows of the constraint matrix C that involve $\mathbf{x}_n$, forming a subset of the original constraints. These rows are removed from the constraint system to form a reduced model. The algorithm computes the projection matrices associated with the reduced and full models, and evaluates the F-statistic. The resulting p-value quantifies the statistical significance of the deviation.

This process is heuristically repeated for each measured phasor, producing a vector of p-values. A binary anomaly flag is set if any of the p-values fall below a specified significance level α. This two-fold output enables both global anomaly detection (i.e., whether any anomaly is present) and identification (i.e., which specific measurements are anomalous).

The complete procedure is summarised in Algorithm Algorithm 1.

Algorithm 1 Anomaly Detection via F-Test

Input: $C, \Sigma_1, \Sigma_2, D, \mathbf{z}, \alpha$
Compute static matrices: $\bar{C}, \bar{\Sigma}, \bar{D}, \bar{G}, \bar{J}, \bar{F}_{11}, \bar{H}, \bar{\mathbf{z}}, \bar{\mathbf{z}}_T, \bar{H}_T$
for each entry in $\mathbf{z}$ **do**
    Identify active rows in C associated with $\mathbf{z}_k$
    Construct reduced constraint set C_1
    Compute $\bar{H}_1, \bar{H}_{1,T}$
    Evaluate F-statistic and compute p-value
    Flag if p-value $< \alpha$
end for
Output: Binary anomaly flag, p-value vector

The algorithms input is the constraint matrix, noise parameters, measurement matrix, measurement vector, and the significance threshold. It computes the static matrices, and then heuristically check if the observed measurement deviates significantly. It returns a binary detection flag and a p-value vector representing the anomaly likelihood of each individual measurement. Each output vector corresponds to a single time instance of synchronised measurements.

4 Evaluation Setup

To assess the performance of the proposed anomaly detection algorithm, we conduct experiments on a calculated dataset based on a MV distribution grid. The test system consists of five nodes in a radial topology, as shown in Figure 1. Node 1 represents the MV busbar at the primary transformer (e.g., 110kV:20kV), and Nodes 3, 4, and 5 are connected through secondary transformers (e.g., 20kV:400V) with downstream loads. All line impedances and grid parameters are specified in Appendix A.11.

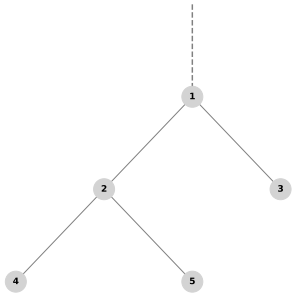

Figure 1: Simple grid structure of the MV distribution grid: Node 1 is the MV side of the primary transformer. Nodes 3, 4, and 5 represent load points behind secondary transformers.

The grid state is generated using distribution load flow calculations [6], resulting in ten phasors: five voltage and five current measurements. These define the ground truth vector $\mathbf{x}$, to which Gaussian noise is added using known covariance structures to produce synthetic measurements $\mathbf{z}$, consistent with the model described in (2). Noise levels follow the assumptions from [10], with a relative error of 1% for voltage magnitude, 3% for current magnitude, and standard deviations of $\sigma_\theta = 0.003$ and $\sigma_\phi = 0.01$ for angular components.

We consider two observability scenarios:

(1) **Fully measured scenario:** All voltage and current phasors are observed.
(2) **Partially measured scenario:** Voltages at Nodes 1 and 2 are omitted. Leaving the remaining eight phasors as observed.

To simulate anomalous conditions, including both accidental faults and cyberattacks, we inject deviations into selected phasors after generating $\mathbf{z}$. The following two types of anomalies are considered:

- **Magnitude multiplier:** The phasor magnitude is multiplied by a scalar (e.g., 1.02 or 1.1).
- **Angle offset:** The phasor angle is perturbed by an additive angle offset (e.g., 1° or 5°).

These anomalies reflect plausible real-world scenarios, and resemble A4 and A5 in [18]. The real world scenarios of magnitude multipliers can arise from misconfigured voltage transformer ratios at measurement devices, a common source of calibration error. Angle offsets, on the other hand, may result from GPS spoofing attacks that disrupt PMU synchronisation, or from local time drift. Both types of deviations are also documented as part of cyberattack scenarios; for example, see the types of anomalies mentioned in [18], especially A4 and A5.

Each anomaly is tested by generating 1,000 samples with added complex Gaussian noise and computing the corresponding F-statistics and p-values for all measured phasors. The significance threshold α is varied across 25 values ranging from 0 to 1 in a fixed sequence: $\alpha \in \{0, 0.01, 0.02, \ldots, 0.05, 0.1, 0.15, \ldots, 1\}$. This allows for evaluating the effect of threshold selection on detection performance.

The performance of the algorithm is based on the following:

- **Sensitivity analysis:** Measures detection rate as a function of anomaly magnitude (e.g., how reliably a 1.02 anomaly is detected compared to 1.1).
- **ROC curves:** Chosen to illustrate the trade-off between true and false positive rates across varying α levels.

For consistency across scenarios, we visualise results for a fixed subset of phasors: Voltage 1 and Voltage 5 (nodal voltages), and $\text{Current}_{0,1}$ and $\text{Current}_{2,5}$ (branch currents). These choices enable direct comparison across anomaly types, magnitudes, and measurement coverage levels. Note that for the partially measured grid scenario, Voltage 1 is removed, and therefore the results for partially measured grids will only display three phasors.

5 Experimental Results

This section presents the results of applying the F-test–based anomaly detection method to the scenarios defined in the evaluation setup. We first examine the sensitivity of the method to varying anomaly magnitude multiplications for a fully measured grid scenario. Then we select specific anomalies and see the results regarding the TPR and FPR tradeoff on ROC curves.

5.1 Sensitivity Analysis

The goal of the sensitivity analysis is to visualise how the two types of anomalies each independently affect the voltage and current phasors. This is applied for a fully measured grid scenario, where Figure 2 shows the detection rate as a function of increasing magnitude multipliers for voltages. The remaining experimental results as described in Section 4 can be found in subsection A.1.

In Figure 2 the magnitude multiplication range from 1.00 to 1.05 in 20 equal increments. Each setting was evaluated with 1000 samples. When no anomaly is applied, i.e. the multiplier is equal to 1.00, the false alarm rate remains close to the nominal significance level of $\alpha = 0.05$, as shown by the dashed lines. This confirms the statistical calibration of the test under normal conditions.

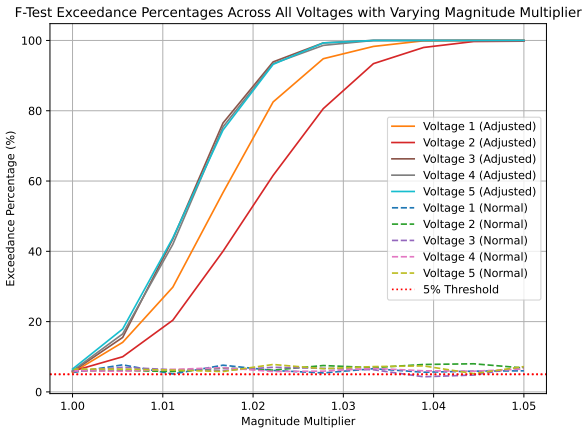

Figure 2: Proportion of rejected F-tests when voltage magnitudes at selected measurement nodes are artificially increased using multiplicative perturbations (solid curves). These multipliers simulate anomalies such as faults or attacks. For comparison, the baseline rejection proportions without perturbations are also shown (dashed curves).

As the multiplier increases, the F-test becomes increasingly sensitive. For most voltages, a multiplier of just 1.03 leads to a average detection rate exceeding 80%, reaching nearly 100% at 1.05. Voltage 2 consistently shows lower sensitivity, though its detection rate still surpasses 80% at 1.03. These results confirm the ability of the F-test to detect even small, physically inconsistent deviations in phasor magnitudes.

5.2 Fully Measured Grid Scenario

We investigate the effect of using different significance levels in the F-test. The results for a fully measured grid scenario, showing Voltage 1 and Voltage 5 along with $\text{Current}_{0,1}$ and $\text{Current}_{2,5}$, for only the magnitude multiplication error are presented in Figure 3 and 4. The two remaining plots, showing the effect of an angle offset for 1° and 5° respectively, can be found in subsection A.2.

To avoid overcrowding the plots, only three significance levels;(α = 0.01, 0.05, and 0.40) are highlighted. The values of 0.01 and 0.05 are commonly selected for statistical testing, while 0.40 provides a broader view of how higher significance levels compare.

For 2% magnitude multiplier, see Figure 3.

At the common significance level $\alpha = 0.05$, the results show strong detection capability with low risk of a false positive. In

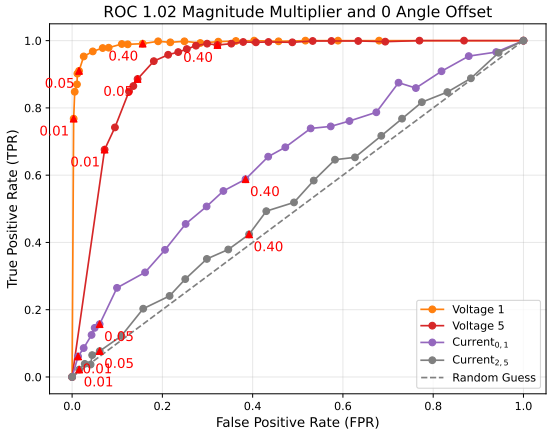

Figure 3: ROC curves for a 2% magnitude increase in the case of a fully measured grid.

contrast, he current measurements display a limited response, especially $\text{Current}_{2,5}$, which performs close to random guessing for this magnitude multiplier of 1.02.

Increasing the multiplier to 10%, see Figure 4.

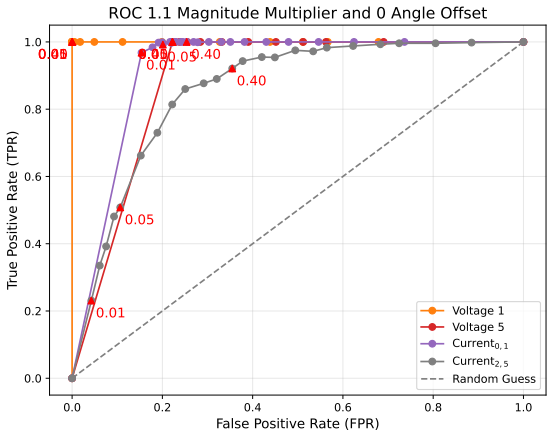

Figure 4: ROC curves for a 10% magnitude increase in the case of a fully measured grid.

The voltage phasors are detected with near-perfect accuracy across all significance levels above 0.1. Notably, the currents also show their trade-off for varying significance levels. The voltage and current connected to node 5 both have a lower TPR and higher FPR for the same significance levels as voltage and current connected to node 1.

5.3 Partially Measured Grid Scenario

The setup is equivalent to the setup in the fully measured grid, however, this partially observed case, Voltage 1 and 2 are excluded from the measurements. We will same display magnitude multipliers, see Figure 5 and Figure 6. The angle offset results for partially measured grid can be found in subsection A.3.

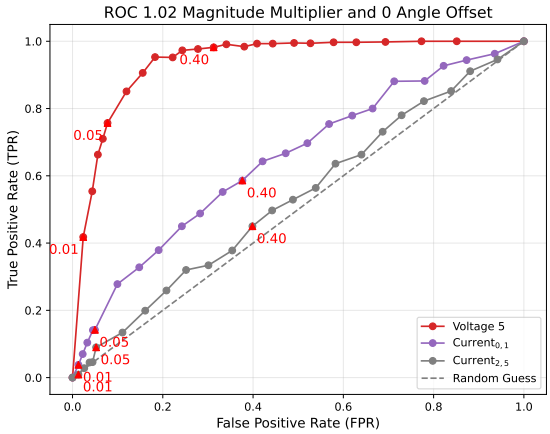

Figure 5: ROC curves for a 2% magnitude increase in the case of a partially measured grid.

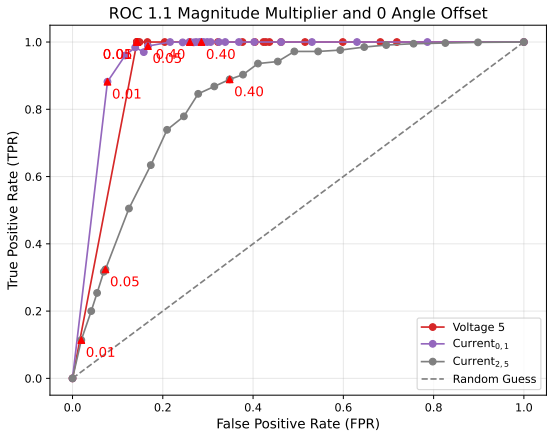

Figure 6: ROC curves for a 10% magnitude increase in the case of a partially measured grid.

At 2%, see Figure 5, voltage 5 is the only phasor who has a decent trade-off. Both currents trade-off are hovering near the random guess indicator.

With a 10% multiplier, see Figure 6. The TPR improves significantly, for all phasors, however, to achieve a high TPR for $\text{current}_{2,5}$, a high significance level must be chosen, allowing the FPR to increase also.

5.4 Scalability

To evaluate the computational feasibility of the proposed method in more realistic settings, we conducted a test on a larger grid consisting of 133 nodes, yielding 266 measurands (voltage and current phasors). A magnitude anomaly of 1.1 was injected into a single measurement, and the detection algorithm correctly identified and localized it. The sequential runtime for a complete evaluation across the grid was approximately 6–7 minutes on a standard workstation laptop. Given that typical medium-voltage grids sampled from 50 European DSOs contain between 100–200 nodes (occasionally up to 500–600), these results confirm the method's practical scalability for real-world deployment.

6 Summary and Outlook

This paper addresses the challenge of detecting anomalies in phasor measurements within medium-voltage distribution grids. By formulating a linear, statistically grounded state-estimation model and applying an F-test framework, the proposed method identifies deviations in both voltage and current measurements that exceed expected measurement noise levels. The framework accommodates two different levels of grid observability, making it applicable to both fully measured and partially measured networks.

The sensitivity analysis confirms that the F-test effectively identifies anomalies in both voltage and current phasors, with detection rates scaling according to the strength of the injected magnitude or angle offsets. Under fully measured conditions, even moderate disturbances such as a 1.03 magnitude multiplier or a 1° additive angle offset, yields an average detection rate, across all samples, of at least 80% for the voltage measurements. On the other hand, identifying current-based anomalies generally requires larger deviations, since current measurements are less sensitive to the chosen anomaly types.

Comparing the fully measured grid scenario with the partially observed scenario, by removing Voltage 1 and Voltage 2, the resulting ROC curves retain a similar pattern for both anomaly types. In spite of the similar pattern, the difference lies in the TPR and FPR trade-off for the same significance levels. The results show a considerably lower TPR and a slightly lower FPR for the same significance levels, indicating the detection model is less confident with fewer measurements.

Overall, the F-test appears efficient and adaptive, offering a statistical framework in which the significance level α can be carefully chosen to balance the trade-off between false positives and missed detections, although reduced measurement coverage seems to reduce the detection confidence of the F-test in terms of reducing the TPR for same significance levels. However, the method's flexibility and clarity in interpreting detection thresholds make it a practical choice for power system monitoring. Moving forward, the F-test's scalability and straightforward applicability to both fully and partially measured grids suggest that it can serve as a solid foundation for broader anomaly detection and system reliability analyses.

There are various possibilities for future extensions of the work in this paper.

First, we have only used a small grid example, and also run some tests on a slightly larger grid. However, some collaborating DSOs to the REDistXAI project have mentioned grids of the size 200+ which would be considered in the future.

Second, we have focused on an idealized version of the distribution networks with only one phase, but for practical applications the system models needs to be generalized to a 3-phase system (see e.g. [4], [9], [13]). All the mathematical results in Section 3 and the appendix remain unchanged, but the matrices needs to be reformulated to fit this case.

Third, we have focused on medium-voltage grids, but the methods are applicable to low-voltage grids as well. Here there is the added issue that such grids are typically measured using cheap smart-meters, only capable of measuring voltage magnitude, current magnitude and the local phase-angle between the voltage and current. One possibility for dealing with the missing global phase-angle is to use the pseudo-measurements introduced in [10], but it is currently unclear how this influences the results of the F-test.

Finally, the proposed anomaly detection algorithm uses multiple tests to detect possible anomalies. This means that we have a multiple testing issue, where α is the significance level for a single test, but it is unclear what the significance level is for the joined tests. Here methods such as Bonferroni corrections may be employed to approximate the overall significance level.

Acknowledgments

The authors gratefully acknowledge funding from the Eurostars-EUREKA Programme under the REDistXAI project. REDistXAI is co-funded by Innovation Fund Denmark and the European Union under grant 3150-00040B / project no. E4748, and by the German Federal Ministry of Education and Research (BMBF) under grant 01QE2419A. We also acknowledge the collaborative contributions from GridData GmbH and thank our colleagues for valuable discussions and technical insights during the development and evaluation of this work.

References

[1] Ahmad N. Alkuwari, Saif Al-Kuwari, and Marwa Qaraqe. 2022. Anomaly Detection in Smart Grids: A Survey From Cybersecurity Perspective. In *2022 3rd International Conference on Smart Grid and Renewable Energy (SGRE)*. IEEE, Doha, Qatar, 1–7. doi:10.1109/SGRE53517.2022.9774221

[2] Reza Arghandeh, Mohini Bariya, George Cotter, Deepjyoti Deka, Dan Dietmeyer, Laurel Dunn, Bryce Johannceck, Christoph Lackner, Panayiotis Moutis, Sai Akhil Reddy Konakalla, Younes Seyedi, Alireza Shasavari, and Anurag Srivastava. 2020. *Synchronized Measurements and their Applications in Distribution Systems: An Update.* Technical Report. North American SynchroPhasor Initiative (NASPI), USA. Available at https://www.naspi.org/.

[3] Bernd M. Buchholz and Zbigniew A. Styczynski. 2020. *Smart Grids: Fundamentals and Technologies in Electric Power Systems of the future.* Springer Berlin Heidelberg, Berlin, Heidelberg. doi:10.1007/978-3-662-60930-9

[4] Wele Gedara Chaminda Bandara, Dilini Almeida, Roshan Indika Godaliyadda, Mervyn Parakrama Ekanayake, and Janaka Ekanayake. 2021. A complete state estimation algorithm for a three-phase four-wire low voltage distribution system with high penetration of solar PV. *International Journal of Electrical Power & Energy Systems* 124 (2021), 106332. doi:10.1016/j.ijepes.2020.106332

[5] Dharmesh Faquir. [n. d.]. Cybersecurity in smart grids, challenges and solutions. 5, 1 ([n. d.]).

[6] J. D. Glover, M. S. Sarma, and T. J. Overbye. 2016. *Power System Analysis and Design* (6th ed.). Cengage Learning, Boston, MA.

[7] J. Jithish, Bithin Alangot, Nagarajan Mahalingam, and Kiat Seng Yeo. 2023. Distributed Anomaly Detection in Smart Grids: A Federated Learning-Based Approach. *IEEE Access* 11 (2023), 7157–7179. doi:10.1109/ACCESS.2023.3237554

[8] Z. Li, Y. Xie, R. Ma, and Z. Wei. 2024. Optimizing CNN-LSTM for the Localization of False Data Injection Attacks in Power Systems. *Applied Sciences* 14, 16 (2024), 6865. doi:10.3390/app14166865

[9] Karthikeyan Nainar and Florin Iov. 2021. Three-Phase State Estimation for Distribution-Grid Analytics. *Clean Technologies* 3, 2 (2021), 395–408. doi:10.3390/cleantechnol3020022
[10] Rasmus L. Olsen, Sina Hassani, Troels Pedersen, Jakob Gulddahl Rasmussen, and Hans-Peter Schwefel. 2024. A Stochastic Approach to Estimate Distribution Grid State with Confidence Regions. *arXiv preprint arXiv:2404.15722* abs/2404.15722, 1 (2024), 29. https://doi.org/10.48550/arXiv.2404.15722 Submitted for publication.
[11] Manikant Panthi. 2020. Anomaly Detection in Smart Grids using Machine Learning Techniques. In *2020 First International Conference on Power, Control and Computing Technologies (ICPC2T)*. IEEE, Raipur, India, 220–222. doi:10.1109/ICPC2T48082.2020.9071434
[12] Jakob G. Rasmussen, Rasmus L. Olsen, Sina Hassani, Troels Pedersen, and Hans-Peter Schwefel. 2024. Selection of Measurements for State Estimation in Electrical Power Distribution Grids. In *IEEE International Conference on Communications, Control, and Computing Technologies for Smart Grids (SmartGridComm)*. IEEE.
[13] Hadi Saadat. 1999. *Power system analysis*. McGraw Hill.
[14] Durgesh Samariya and Amit Thakkar. 2021. A Comprehensive Survey of Anomaly Detection Algorithms. *Annals of Data Science* 8, 4 (2021), 897–930. doi:10.1007/s40745-021-00362-9
[15] Peter J. Schreier and Louis L. Scharf. 2010. *Statistical Signal Processing of Complex-Valued Data: The Theory of Improper and Noncircular Signals*. Cambridge University Press.
[16] Jiuqi Elise Zhang, Di Wu, and Benoit Boulet. 2021. Time Series Anomaly Detection for Smart Grids: A Survey. http://arxiv.org/abs/2107.08835 arXiv:2107.08835 [cs].
[17] Mehdi Jabbari Zideh and Sarika Khushalani Solanki. 2024. Multivariate Physics-Informed Convolutional Autoencoder for Anomaly Detection in Power Distribution Systems with High Penetration of DERs. *arXiv preprint arXiv:2406.02927* (2024). https://arxiv.org/abs/2406.02927
[18] Tommaso Zoppi, Irene Bicchierai, Francesco Brancati, Andrea Bondavalli, and Hans-Peter Schwefel. 2024. Deploying a Generic Threat Model for Detecting Anomalies in a Power Grid Digital Twin. In *2024 IEEE 29th Pacific Rim International Symposium on Dependable Computing (PRDC)*. IEEE, Osaka, Japan, 208–215. doi:10.1109/PRDC63035.2024.00039

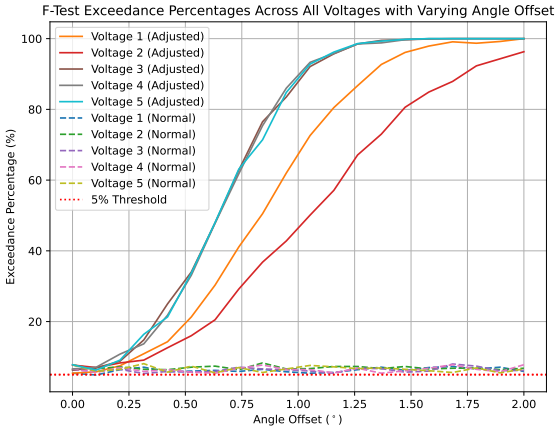

Figure 7: Proportion of rejected F-tests for varying voltage angle offsets applied to different voltage measurement locations (solid curves). For comparison the proportions are also shown without offsets (dashed curves).

A Appendix

This appendix primarily includes rigorous mathematical derivation, data description, and extra results which further enhance the current results.

A.1 Sensitivity analysis results

This subsection presents the remaining sensitivity analysis results, beginning with the node voltages sensitivity regarding phase angle offset which can be seen in Figure 7. The corresponding analysis for the line currents is shown in Figure 8 and Figure 9, for magnitude multiplication and angle offset, respectively.

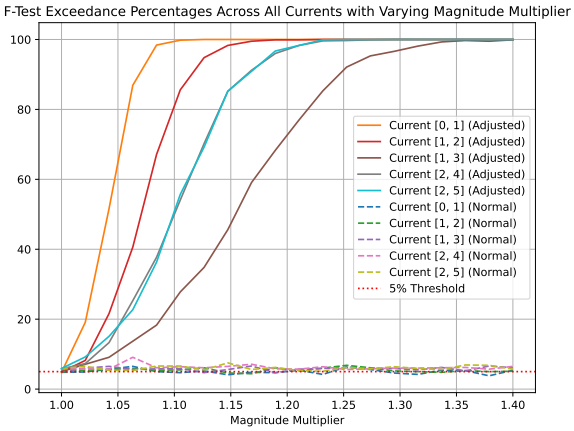

Figure 8: Proportion of rejected F-tests for varying current magnitude multipliers applied to different current measurement locations (solid curves). For comparison the proportions are also shown without multipliers (dashed curves).

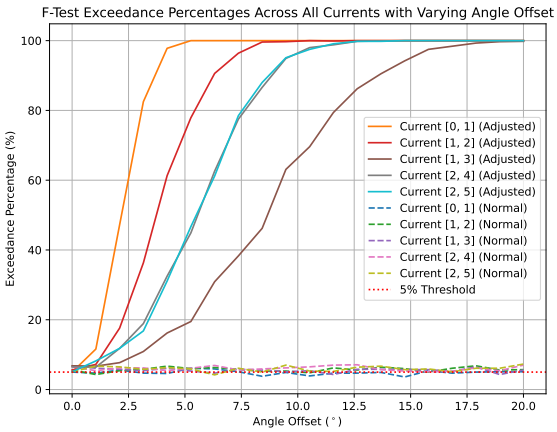

Figure 9: Proportion of rejected F-tests for varying current angle offsets applied to different current measurement locations (solid curves). For comparison the proportions are also shown without offsets (dashed curves)

A.2 Fully measured grid scenario: angle offset results

Two additive angle offsets are explored in Figures 10 and 11. These plots mirror the patterns observed under small and large magnitude multipliers, respectively, but now in the context of angle deviations instead of magnitude changes.

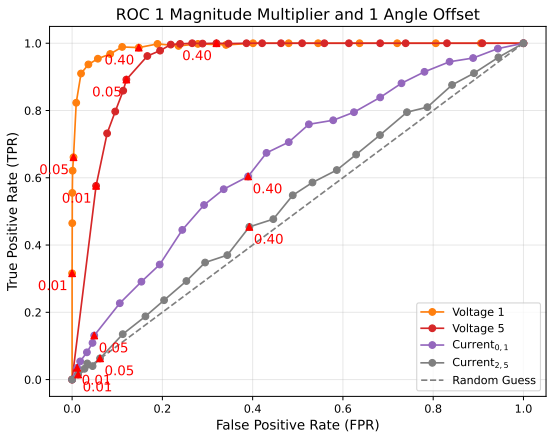

Figure 10: ROC curves for a 1° angle offset in the case of a fully measured grid.

At a 1° offset (see Figure 10), the voltages quickly achieve high TPR values at relatively low significance levels α, whereas the currents exhibit weaker detection capabilities and an unfavorable tradeoff between TPR and FPR, closely reflecting the behavior seen in Figure 3 for small magnitude anomalies.

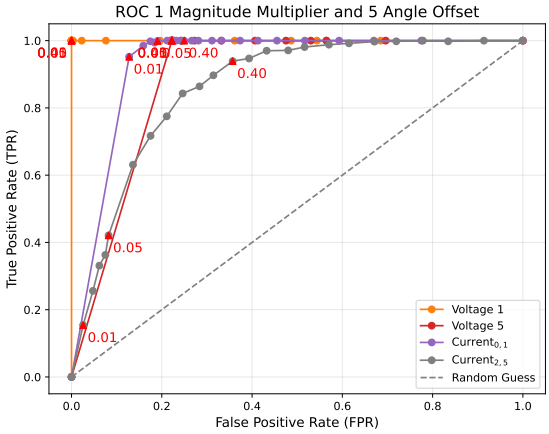

Figure 11: ROC curves for a 5° angle offset in the case of a fully measured grid.

When the angle offset increases to 5° (see Figure 11), a marked improvement in current-based detection is observed, paralleling the stronger response noted for larger magnitude anomalies in Figure 4. Voltage measurements also maintain high TPR values, underscoring their sensitivity to even moderate angle deviations.

A.3 Partially measured grid scenario: angle offset results

Exact same setup as the fully measured grid, except that the measurements of voltages at nodes 1 and 2 are omitted.

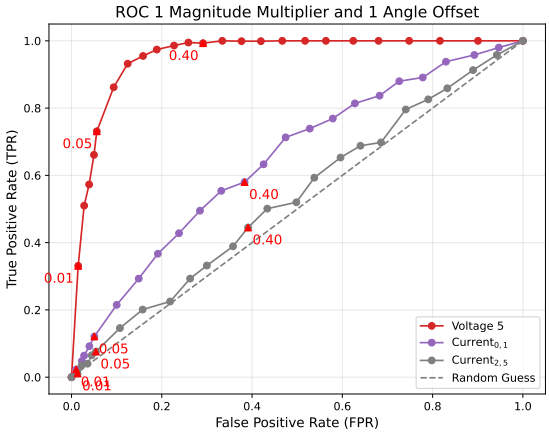

Figure 12: ROC curves for a 1° angle offset in the case of a partially measured grid.

The angle offsets of 1° (Figure 12) and 5° (Figure 13) closely parallel the patterns observed for magnitude multipliers of 1.02 and 1.1, respectively.

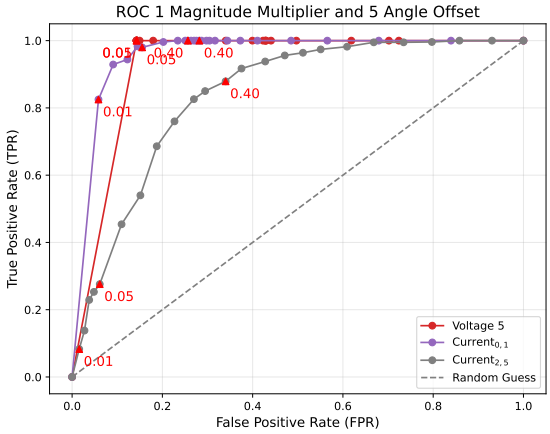

Figure 13: ROC curves for a 5° angle offset in the case of a partially measured grid.

A.4 Overview of Notation and Setup for $\bar{H}$

To compute the matrices required for the F-test, we follow these three steps, which are based on [10].

- First, we define the grid setup and data generation:
  - Define the physical grid structure, which determines the constraint matrix C.
  - Specify the true grid state $\mathbf{x} \in \mathbb{C}^N$ and noise assumptions, which are used to derive the covariance matrices Σ_1 and Σ_2.
  - Determine the observation structure (e.g., which nodes or lines are measured) via the matrix $D \in \{0,1\}^{K\times N}$, leading to the observed measurements $\mathbf{z} \in \mathbb{C}^K$.
- Secondly, we adopt the complex-augmented formulation to streamline derivations:
  - Define the augmented vector and matrix:

$$\bar{\mathbf{v}} = \begin{pmatrix} \mathbf{v} \\ \mathbf{v}^* \end{pmatrix}, \qquad \overline{(B_1, B_2)} = \begin{pmatrix} B_1 & B_2 \\ B_2^* & B_1^* \end{pmatrix},$$

    where $\mathbf{v} \in \mathbb{C}^n$, and $B_1, B_2 \in \mathbb{C}^{m\times n}$. This leads to:

$$\bar{C} = \overline{(C, O)}, \qquad \bar{D} = \overline{(D, O)},$$

    with O denoting a context-dependent zero matrix.
  - Key matrix construction:
    - Define the covariance-derived matrices:

$$P = \Sigma_1^* - \Sigma_2^H \Sigma_1^{-1} \Sigma_2,$$
$$W = \Sigma_2 (\Sigma_1^*)^{-1},$$

      and then construct the augmented matrix:

$$\bar{G} = \overline{\left(2D^H (P^*)^{-1} D,\ -2D^H (P^*)^{-1} W D^*\right)}.$$

    - Define the block matrix:

$$A = \begin{pmatrix} \bar{G} & \bar{C}^H \\ \bar{C} & O \end{pmatrix} \in \mathbb{C}^{2(N+Q)\times 2(N+Q)},$$

    which is assumed to be invertible. Its inverse is partitioned as:

$$A^{-1} = \begin{pmatrix} \bar{F}_{11} & \bar{F}_{12} \\ \bar{F}_{21} & \bar{F}_{22} \end{pmatrix}.$$

    - The maximum likelihood estimate of the augmented state is then:

$$\hat{\bar{\mathbf{x}}} = \bar{F}_{11}\bar{\mathbf{g}}, \quad \text{where } \bar{\mathbf{g}} = \overline{(\mathbf{g}, \mathbf{g}^*)}, \quad \mathbf{g} = 2D^H (P^*)^{-1}(\mathbf{z} - W\mathbf{z}^*).$$

- Lastly, we define the projection formulation:
  - Project the data $\bar{\mathbf{z}}$ onto the estimated state:

$$\hat{\bar{\mathbf{z}}} = \bar{D}\bar{F}_{11}\bar{J}\bar{\mathbf{z}},$$

    where

$$\bar{J} = \overline{\left(2D^H (P^*)^{-1},\ -2D^H (P^*)^{-1} W\right)}.$$

  - Define the projection matrix:

$$\bar{H} = \bar{D}\bar{F}_{11}\bar{J}, \tag{5}$$

    which is used in the F-test statistic. As shown in [12], $\bar{H}$ is an oblique projection. However, in subsection A.5 it is shown how it becomes orthogonal in a simple covariance scenario.

A.5 Proof that $\bar{H}$ is an orthogonal projection

Lemma A.1. *If $\Sigma_1 = I$ and $\Sigma_2 = O$, then $\bar{H}$ is an orthogonal projection.*

Proof. To verify that $\bar{H}$ is an orthogonal projection, we need to verify that it is idempotent and Hermitian, where idempotency is already verified in [12].

Since $\bar{H} = \bar{D}\bar{F}_{11}\bar{J}$, we want to show that this product is hermitian. Inserting $\Sigma_1 = I$ and $\Sigma_2 = O$ into the definition of $\bar{J}$, we get that $\bar{J} = 2\bar{D}^H$, and thus

$$\bar{H} = 2\bar{D}\bar{F}_{11}\bar{D}^H. \tag{6}$$

Using Proposition A.3, we now need to verify that $\bar{F}_{11}$ is Hermitian. For this, firstly observe that $P_{\bar{C}}$ is an orthogonal projection, and therefore it is also Hermitian.

Secondly, inserting $\Sigma_1 = I$ and $\Sigma_2 = O$ into $\bar{G}$, we get that $\bar{G} = 2\overline{(D^H D, O)}$, and since $D^H D$ is Hermitian, $\bar{G}$ is also Hermitian. Hence

$$\bar{F}_{11}^H = ((P_{\bar{C}}\bar{G}P_{\bar{C}})^+)^H = (P_{\bar{C}}^H \bar{G}^H P_{\bar{C}}^H)^+ = (P_{\bar{C}}\bar{G}P_{\bar{C}})^+ = \bar{F}_{11},$$

and therefore $\bar{F}_{11}$ is Hermitian.

Finally, using (6), we get that $\bar{H}$ is Hermitian, since

$$\bar{H}^H = (2\bar{D}\bar{F}_{11}\bar{D}^H)^H = 2(\bar{D}^H)^H \bar{F}_{11}^H \bar{D}^H = 2\bar{D}\bar{F}_{11}\bar{D}^H = \bar{H},$$

which means that $\bar{H}$ is an orthogonal projection. □

A.6 Proof of F-test under simple covariance assumption

This subsection explains the F-test under simple covariance assumptions, which results in a lemma that will be used to prove Proposition 3.1 for the general covariance structure.

Lemma A.2. *Assume that* (2) *and* (1) *holds. If* $\Sigma_1 = I$ *and* $\Sigma_2 = O$, *then under* $\mathcal{H}_0$

$$F(\mathbf{z}) = \frac{\|\bar{H}_1\bar{\mathbf{z}} - \bar{H}\bar{\mathbf{z}}\|^2/\delta_1}{\|\bar{\mathbf{z}} - \bar{H}_1\bar{\mathbf{z}}\|^2/\delta_2} \tag{7}$$

follows an F-distribution with degrees of freedom given by

$$\delta_1 = 2Q_0 \quad \textit{and} \quad \delta_2 = 2(K + Q_1 - N).$$

Proof. To show that $F(\mathbf{z}) \sim F_{\delta_1,\delta_2}$ under H_0, we need to show that the squared norms in the numerator and the denominator follow independent χ^2-distributions with δ_1 and δ_2 degrees of freedom.

To prove this a few geometric considerations are in order. Firstly, by Lemma A.1 both $\bar{H}$ and $\bar{H}_1$ are orthogonal projections. Secondly, we are removing restrictions when going from $\bar{H}$ to $\bar{H}_1$, meaning that $\bar{H}_1$ is projecting unto a larger subspace than $\bar{H}$, i.e. the column space of $\bar{H}$ is a subspace of the column space of $\bar{H}_1$. This implies that $\bar{H}\bar{H}_1 = \bar{H}_1\bar{H} = \bar{H}$ and that $\bar{H}_1 - \bar{H}$ is an orthogonal projection.

Now the squared norm in the numerator can be expressed as

$$\|(\bar{H}_1 - \bar{H})\bar{\mathbf{z}}\|^2 = \bar{\mathbf{z}}^H(\bar{H}_1 - \bar{H})^H(\bar{H}_1 - \bar{H})\bar{\mathbf{z}} = \bar{\mathbf{z}}^H(\bar{H}_1 - \bar{H})\bar{\mathbf{z}}, \tag{8}$$

since $\bar{H}_1 - \bar{H}$ is an orthogonal projection. Using Cochran's theorem, we get that the quadratic form in (8) follows a χ^2-distribution with

$$\delta_1 = \operatorname{rank}(\bar{H}_1 - \bar{H}) = \operatorname{rank}(\bar{H}_1) - \operatorname{rank}(\bar{H}) = (N - Q) - (N - Q_1) = Q_0$$

degrees of freedom, where we have used Proposition 1 from [12] for obtaining the ranks.

Similarly it can be shown that $\|\bar{\mathbf{z}} - \bar{H}_1\bar{\mathbf{z}}\|^2$ follows a χ^2-distribution with $2(K - Q_1 - N)$ degrees of freedom.

Finally, the independence of the numerator and denominator follows from Cochran's theorem using

$$(I - \bar{H})(\bar{H}_1 - \bar{H}) = I\bar{H}_1 - I\bar{H} - (\bar{H}_1)^2 + \bar{H}_1\bar{H} = O.$$

Hence, the squared norms in the numerator and denominator are independent χ^2 distributions, each divided by the respective degrees of freedom, and therefore (7) follows an F-distribution with δ_1 and δ_2 degrees of freedom. □

A.7 Transformation matrix T

This subsection essentially describes how Lemma A.2 can be transformed into Proposition 3.1. The trick to making this work is to transform the case of arbitrary covariance and pseudo-covariance matrices back to the simplified case from Section A.6.

Reformulating (2) into the equivalent augmented form, i.e. let $\bar{\Sigma} = \overline{(\Sigma_1, \Sigma_2)}$ and

$$\bar{\mathbf{z}} = \bar{D}\bar{\mathbf{x}} + \bar{\boldsymbol{\epsilon}}, \qquad \bar{\boldsymbol{\epsilon}} \sim CN(0, \bar{\Sigma}),$$

we can transform this equation into

$$\bar{\mathbf{z}}_T = \bar{D}_T\bar{\mathbf{x}} + \bar{\boldsymbol{\epsilon}}_T, \qquad \bar{\boldsymbol{\epsilon}}_T \sim CN(0, I), \tag{9}$$

where $T = \bar{\Sigma}^{-\frac{1}{2}}$ is the inverse of a square root of $\bar{\Sigma}$, and we have denoted $\bar{\mathbf{z}}_T = \bar{T}\mathbf{z}$, $\bar{D}_T = T\bar{D}$ and $\bar{\boldsymbol{\epsilon}}_T = T\bar{\boldsymbol{\epsilon}}$. Since $\bar{\Sigma}$ is Hermitian and positive definite, we can use the unique root which is also Hermitian and positive definite, i.e. the principal square root, which for example can be obtained using Eigenvalue decomposition.

A.8 Proof for F-test under abritrary covariance assumption

Here we give the proof of Proposition 3.1:

Proof. Observe that the principal square root preserves the augmented form; this can be seen by using the power expansion for the square root, i.e.

$$\bar{\Sigma}^{\frac{1}{2}} = \sum_{n=0}^{\infty}(-1)^n\binom{\frac{1}{2}}{n}(I - \bar{\Sigma})^n,$$

together with the fact that sums, multiplications, and real-valued scalar multiplications preserve the augmented form [15]. Since inverses also preserve the augmented form, it follows that T is on augmented form, and therefore all terms in (9) are on augmented form. So (9) is equivalent to the simple case considered in Lemma A.2. Thus since

$$\hat{\bar{\mathbf{z}}}_T = T\hat{\bar{\mathbf{z}}} = T\bar{H}\bar{\mathbf{z}} = T\bar{H}T^{-1}\bar{\mathbf{z}}_T,$$

we get that the projection matrix for the transformed case is given by

$$\bar{H}_T = T\bar{H}T^{-1},$$

and a similar result holds for $\bar{H}_{1,T}$. Inserting $\bar{\mathbf{z}}_T$, $\bar{H}_T$ and $\bar{H}_{1,T}$ into Lemma A.2, we get the result. Note that the degrees of freedom are same as in Lemma A.2, as the transformation does not change the rank of the projection matrices. □

A.9 Requirements for applying the F-test

This subsection describes when the F-test is not applicable, i.e. we need a sufficient amount of data to use it. Here two requirements need to be fulfilled.

First, we need to be able to uniquely estimate the true state using the data and the reduced constraint matrix C_1, which by Proposition 3 in [12] is possible if

$$\operatorname{rank}\left(\begin{bmatrix} D \\ C_1 \end{bmatrix}\right) = N. \tag{10}$$

This is equivalent to $\bar{H}_1$, and thus $H_{1,T}$, being well-defined.

Second, we need to ensure that the degrees of freedom are positive. While δ_1 is always positive, δ_2 is positive if and only if the number of measurements fulfills $K > N - Q_1$. Note that this excludes the case where we have the minimal amount of data needed to estimate under the constraints implied by C_1, since by Proposition 1 in [12] we then have $K = N - Q_1$. Intuitively, it means that we need to have enough measured phasors so that the measurements at the different grid locations contain enough 'redundancy' to reason about the presence of anomalies.

A.10 Formula for $\bar{F}_{11}$

The matrix $\bar{F}_{11}$ is vital for establishing the results in this paper. As mentioned in [10], it is easy to obtain $\bar{F}_{11}$ numerically by inverting A and extracting the appropriate block, but the following result establishes an alternative way of calculating it, using the Moore-Penrose inverse denoted by $^+$.

Proposition A.3. *Given* A *and* A^{-1} *from [10], it holds that*

$$\bar{F}_{11} = (P_{\bar{C}}\bar{G}P_{\bar{C}})^+,$$

where $P_{\bar{C}} = I - \bar{C}^H(\bar{C}\bar{C}^H)^{-1}\bar{C}$ is the projection matrix onto the orthogonal complement of the column space of $\bar{C}$.

Proof. We start by rewriting the block structure of A into

$$A = \begin{bmatrix} B_1 & B_2 \end{bmatrix}, \quad B_1 = \begin{bmatrix} \bar{G} \\ \bar{C} \end{bmatrix}, \quad B_2 = \begin{bmatrix} \bar{C}^H \\ O \end{bmatrix}.$$

Now using that the usual matrix inverse is equal to the Moore-Penrose for invertible matrices, we can use the block inverse formulas for the Moore-Penrose inverse to get

$$A^{-1} = A^+ = \begin{bmatrix} B_1 & B_2 \end{bmatrix}^+ = \begin{bmatrix} (P_{B_2}B_1)^+ \\ (P_{B_1}B_2)^+ \end{bmatrix} \Rightarrow \begin{bmatrix} \bar{F}_{11} & \bar{F}_{12} \end{bmatrix} = (P_{B_2}B_1)^+$$

where P_{B_1} and P_{B_2} denote orthogonal projection matrices onto the orthogonal complements of the column spaces of matrices B_1 and B_2, respectively. Expanding $P_{B_2}B_1$, we find:

$$\begin{aligned} P_{B_2}B_1 &= (I - B_2(B_2^H B_2)^{-1}B_2^H)B_1 \\ &= \left(I - \begin{bmatrix} \bar{C}^H \\ O \end{bmatrix}\left(\begin{bmatrix} \bar{C} & O \end{bmatrix}\begin{bmatrix} \bar{C}^H \\ O \end{bmatrix}\right)^{-1}\begin{bmatrix} \bar{C} & O \end{bmatrix}\right)\begin{bmatrix} \bar{G} \\ \bar{C} \end{bmatrix} \\ &= \begin{bmatrix} P_{\bar{C}}\bar{G} \\ \bar{C} \end{bmatrix}. \end{aligned}$$

Then taking the Moore-Penrose inverse, again using block inverse formulas, yields

$$(P_{B_2}B_1)^+ = \begin{bmatrix} P_{\bar{C}}\bar{G} \\ \bar{C} \end{bmatrix}^+ = \begin{bmatrix} (P_{\bar{C}}\bar{G}P_{\bar{C}})^+ & (\bar{C}P_{P_{\bar{C}}\bar{G}})^+ \end{bmatrix}$$

where the first entry corresponds to

$$\bar{F}_{11} = (P_{\bar{C}}\bar{G}P_{\bar{C}})^+,$$

which concludes the proof. □

A.11 Data for the MV Grid

This subsection presents the data used for the small grid in the experiments. The tables provide sufficient information to reconstruct the state vector $\mathbf{x}$, system matrix D, noise covariances Σ_1, Σ_2, and the constraint matrix C, assuming the grid topology is known.

Table 1: Combined Data for Medium Voltage Distribution Grid

Index	Impedance (Z)	Voltage [V]	Current [A]
1	Not specified	$20000.00 + 0.00i$	$15541.46 - 3225.61i$
2	$0.07 + j0.03$	$19318.73 - 130.00i$	$10444.02 - 2185.01i$
3	$0.02 + j0.01$	$19601.77 - 78.00i$	$5097.44 - 1040.60i$
4	$0.08 + j0.01$	$19114.35 - 169.00i$	$5222.01 - 1092.50i$
5	$0.08 + j0.01$	$19114.35 - 169.00i$	$5222.01 - 1092.50i$

To reproduce the algorithm, perform your own experiments, or extend the method, a minimal and readable implementation of the code is publicly available on GitHub:

`https://github.com/DauselJensen/F-testcode`